

Investigation of the Effect of Alloying Elements and Water Vapor Contents on the Oxidation and Decarburization of Transformation-Induced Plasticity Steels

Z.T. ZHANG, I.R. SOHN, F.S. PETTIT, G.H. MEIER, and S. SRIDHAR

The present research deals with an investigation of the effect of alloying element additions (Si, P, and Sb) and water vapor content ($P_{H_2O}/P_{H_2} = 0.01$ to 0.13) on the oxidation and decarburization behavior of transformation-induced plasticity (TRIP) steels in a gas mixture of 95 vol pct argon and 5 vol pct hydrogen/steam, by thermogravimetry (TG). The oxidation proceeds primarily as an internal oxidation front in the TRIP steels, but a thin external scale on the order of a micrometer thickness exists and is comprised primarily of fayalite ($(Mn,Fe)_2SiO_4$) and $((MnO)_x(FeO)_{1-x})$. The oxidation products are distributed near the surface and along grain boundaries. A comparison between calculated and measured oxidation curves indicated that the oxidation and decarburization are independent. The results for TRIP steels, both with and without an Sb addition, indicate that increasing Si and P contents accelerate, whereas Sb addition suppresses, both decarburization and oxidation rates. Water vapor content has no obvious effect on decarburization but has a pronounced effect on oxidation, and decreasing water vapor content decreases the oxidation rates.

DOI: 10.1007/s11663-009-9255-x

© The Minerals, Metals & Materials Society and ASM International 2009

I. INTRODUCTION

TRANSFORMATION-INDUCED plasticity (TRIP) steels are among the most ideal candidates for light-weight automotive applications because of their high strength-to-weight ratio and excellent deformability.^[1-3] In order to obtain these properties, TRIP steels have conventionally contained C, Mn, P, and Si, of which C and Mn are used to stabilize austenite and Si and P are used as solid-solution strengtheners and to suppress iron carbide formation.^[4-6] The Al plays a role similar to that of Si in TRIP steels and can partially replace Si in view of the detrimental effect of Si, because silicon contents above 0.1 pct do not permit the formation of a uniform galvanized product, while aluminum does not have a detrimental effect on the galvanizing process.^[7-10] The application of a zinc coating is an important factor to consider in producing products with acceptable surface

quality for the automotive industry. To achieve a uniformly coated surface, it is necessary to control surface oxidation before hot-dip galvanizing such that the oxidation products allow the coating alloy to wet the surface. During the heat-treatment process, small amounts of alloying elements that are commonly used in TRIP steels, such as Si, Mn, and Al, are selectively oxidized. Some of the oxides based on Mn or Si are undesirable.^[11] To improve the wettability of TRIP steels, some researchers tried to suppress the oxidation by adding some surface active elements, one of which is Sb. An addition of Sb has been found to significantly affect the recrystallization of steels^[12] and to suppress internal oxidation,^[13] as well as to improve the texture of nonoriented Si steels. This was due to the formation of a texture rich in (100) grains in Si steels caused by the presence of Sb.^[14,15] In addition, Sb is expected to suppress the decarburization of TRIP steels due to its high segregation tendency.

In earlier articles from the present research group, the authors investigated the oxidation of TRIP and interstitial-free (IF) steels through thermogravimetry (TG) and confocal scanning laser microscopy methods.^[13,16,17] The articles elucidated the evolution of internal oxidation, external oxidation, and decarburization and their interdependence under different P_{H_2O}/P_{H_2} ratios for TRIP steels, and the effect of water vapor content, temperature, and alloying elements on the oxidation of IF steels. It was found that Si increases the internal oxide density and causes Fe extrusion to the surface, and that Sb addition suppresses both the internal and external oxidation of IF steels. An increase in P content slightly increases the internal oxidation of IF steels. However, the effect of alloying element

Z.T. ZHANG, formerly Research Associate, Department of Materials Science and Engineering, Carnegie Mellon University, is Associate Professor, Department of Energy and Resources Engineering, College of Engineering, Peking University, Beijing, 100871, People's Republic of China. S. SRIDHAR, POSCO Professor of Steelmaking, Department of Materials Science and Engineering, Carnegie Mellon University, Pittsburgh, PA 15213, is with the National Energy Technology Laboratory, Pittsburgh, PA 15236. Contact e-mail: sridhars@andrew.cmu.edu I.R. SOHN, Senior Research Engineer, is with Technical Research Labs., POSCO, Jeonnam 545-090, Korea. F.S. PETTIT, Professor Emeritus, is with the Department of Mechanical Engineering and Materials Science, University of Pittsburgh, Pittsburgh, PA 15260. G.H. MEIER, Professor, Department of Mechanical Engineering and Materials Science, University of Pittsburgh, is with the National Energy Technology Laboratory.

Manuscript submitted November 14, 2008.

Article published online July 3, 2009.

additions on the oxidation and decarburization in TRIP steels has not been reported so far. The objective in the current study is to investigate the roles of P, Si, and Sb as well as the effect of water vapor content in the oxidizing gas on the decarburization and oxidation of TRIP steels.

II. EXPERIMENTAL PROCEDURE

The TRIP steels used in the present study were supplied by POSCO (Jeonnam, Korea) and were fabricated by casting from a vacuum furnace into steel molds $170 \times 230 \times 60$ (mm) in thickness and then hot rolling in nine passes to a thickness of 3 mm. The hot-rolled strips were then pickled and cold-rolled five passes to a final thickness of 2 mm. Table I shows the chemical compositions. Coupons were cut, ground, and polished into pieces $20 \times 6 \times 2$ (mm) in size, for use in the TG experiments. A typical etched surface microstructure before oxidation is shown in Figure 1. It can be seen that the TRIP specimen consists primarily of ferrite regions (appearing dark) and layers or bands of pearlite regions (appearing light). The gases used in the present experiment are argon and hydrogen gases, which were provided by Valley National Gases, Inc. (Wheeling, WV).

The experimental procedures have been described in an earlier article,^[13,17] and will be briefly summarized here. A TG analysis setup (SETARAM Instrumentation,

Caluire, France) was mainly used in the present experiments. The experimental atmosphere was controlled by a gas mixture that consists of 95 vol pct argon and 5 vol pct hydrogen, and the hydrogen gas flowed through a well-defined humidifier. The gas-flow rates for the dry (Ar) and wet ($H_2 + H_2O$) gas streams were 190 and 10 mL/min, respectively, corresponding to linear flow rates of 0.6 and 0.03 m/min, respectively. It should be noted that the flow rates used were such that the gas stream was not starved of oxidant as a result of oxidation of the metal, and the mass transfer of water vapor from the bulk gas to the surfaces of specimens and the dissociation of water vapor were not rate-limiting steps.^[13] The buoyancy effect has been evaluated in a previous article,^[17] and the results show that it can be ignored at the oxidation temperature. The furnace was heated from room temperature to the exposure temperature (843 °C) at a heating rate of 99 °C/min, and held for a certain time, then cooled at a cooling rate of 99 °C/min. The exposure temperature (843 °C) is located on the lower-temperature boundary of the austenite region at low carbon contents, *i.e.*, the $\alpha/\alpha + \gamma$ boundary. Table II gives the experimental conditions and the corresponding oxygen partial pressures used in the present experiments. Figure 2 shows the thermal history used. It should be pointed out that recrystallization is completed before the experimental temperatures are reached. The recrystallization is, therefore, not considered in the present experiments.

The exposed specimens were characterized by glancing-angle X-ray diffraction (G-XRD), a scanning electron microscope (SEM) equipped with an energy-dispersive X-ray detector (EDS) (INCA, Oxford Instruments, Scotts Valley, CA), X-ray photoelectron spectroscopy (XPS), optical microscopy (OM), and Auger electron mapping system (AES) techniques. The detailed experimental procedures of G-XRD, SEM-EDS, and XPS have been described in an earlier article.^[13] Therefore, only the experimental procedures for AES will be described here. The AES was used to map the surface element distribution. The voltage and current of the electron beam for the AES analysis were 10 kV and 5 μ A, respectively. Other parameters employed in the present experiments were 4 kV and 15 mA, as the voltage of the argon ion gun and the emission current, respectively. A cylindrical mirror analyzer with a coaxial electron gun at normal incidence was used to record the Auger spectra. In order to get a proper quantification of the Auger spectra, the distance and angle between the specimen and analyzer axis should be maintained fixed. This angle was maintained at 30 deg during the period of the experiment.

Table I. Chemical Compositions of TRIP Steels

Sample	Chemical Compositions (Wt Pct)						
	C	Si	Mn	P	S	Al	Sb
1	0.2	0.5	2.0	0.02	0.002	0.5	—
2	0.2	0.5	2.0	0.08	0.002	0.5	—
3	0.2	1.0	2.0	0.02	0.002	0.5	—
4	0.2	1.5	2.0	0.02	0.002	0.5	—
5	0.2	0.5	2.0	0.02	0.002	0.5	0.03
6	0.2	0.5	2.0	0.08	0.002	0.5	0.03
7	0.2	1.0	2.0	0.02	0.002	0.5	0.03
8	0.2	1.5	2.0	0.02	0.002	0.5	0.03

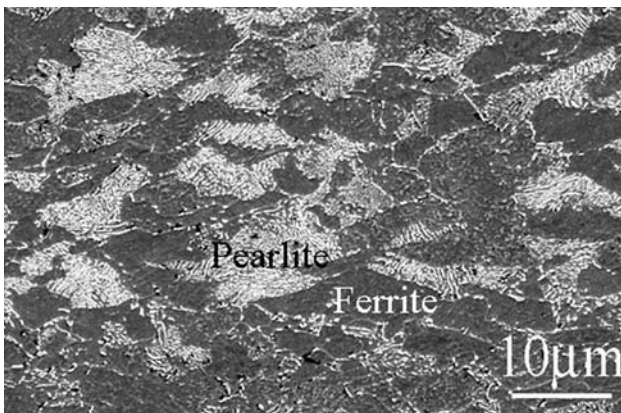


Fig. 1—Typical surface morphology of TRIP steel 2 etched with nital for 30 s. Dark regions are ferrite; light regions are pearlite.

III. RESULTS AND DISCUSSION

A. Thermogravimetric Analysis

The TG curves for specimens oxidized under $P_{H_2O}/P_{H_2} = 0.13$ have the general appearance of those shown in Figures 3 and 4, in which there is a weight loss due to the dominance of the rapid rate of decarburization over the rate of oxidation. In order to establish the

Table II. Measured Depths of Decarburization and Internal Oxidation Layers of TRIP Steels Oxidized at 843 °C

Item	P_{H_2O}/P_{H_2}	$\log(P_{O_2})$ (atm)	Sample 1	Sample 2	Sample 3	Sample 4	Sample 5	Sample 6	Sample 7	Sample 8
Decarburization depth (μm)	0.13	-19.17	73.9	96.8	99.1	152.1	51.8	88.6	60.9	78.5
	0.06	-19.84	67.3	—	—	—	—	—	—	—
	0.01	-21.40	58.5	—	—	—	—	—	—	—
Oxide depth (μm)	0.13	-19.17	8.3	9.9	5.2	6.3	2.5	4.9	3.5	2.6
	0.06	-19.84	7.4	—	—	—	2.4	—	—	—
	0.01	-21.40	6.7	—	—	—	1.8	—	—	—

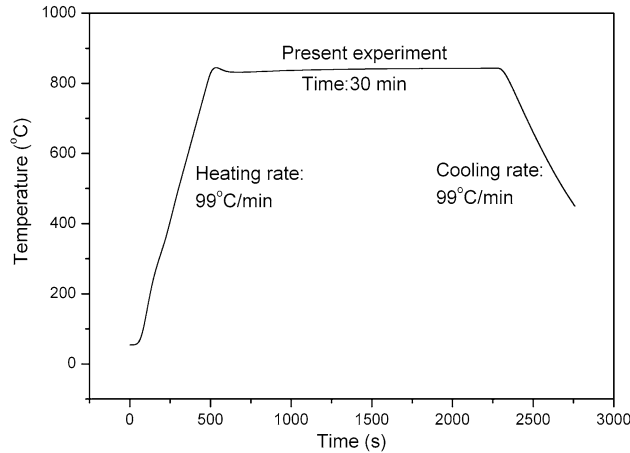


Fig. 2—Schematic of thermal history.

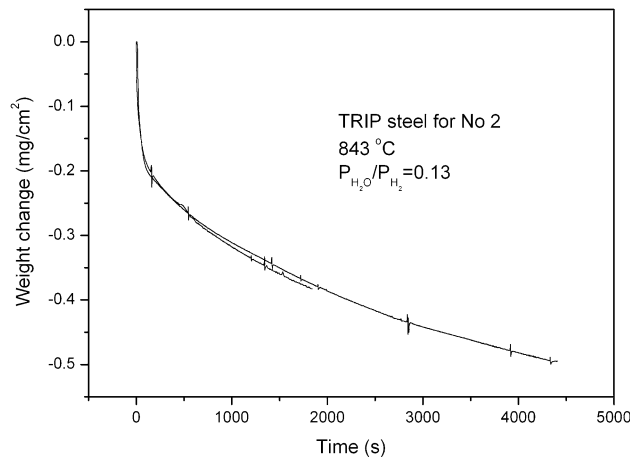


Fig. 3—Repeatability of the decarburization experiments for TRIP steel 2.

reproducibility of the experimental results, selected experiments were repeated. Figure 3 gives the experimental results of two experiments carried out under the same conditions in terms of specimen temperature and atmosphere but for different times. As can be seen, the results have good repeatability.

Figure 4 shows the weight changes of TRIP steels with different chemical compositions as a function of the oxidation time, indicating that alloying element additions have significant effects on decarburization or oxidation. The numbers labeled in the figures correspond to the compositions in Table I. It should be pointed out that decarburization and oxidation occur

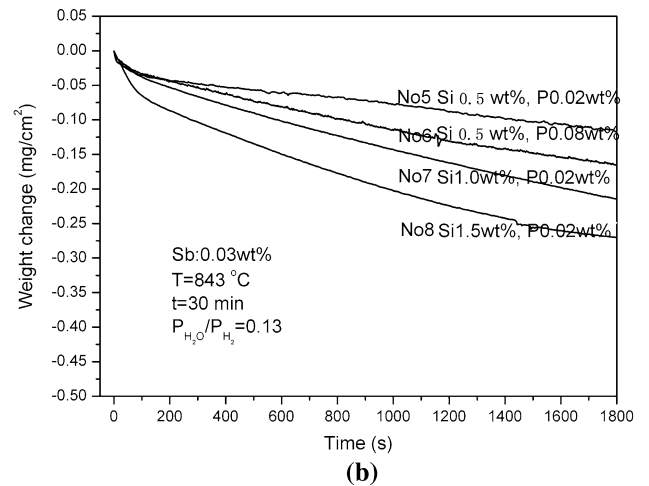
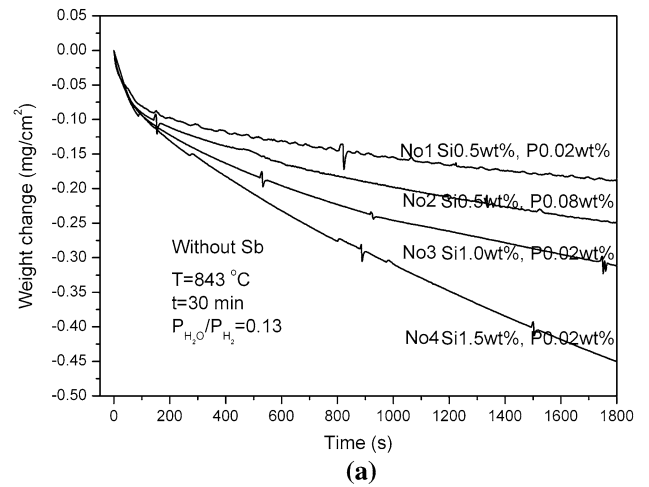


Fig. 4—Weight changes of TRIP steels containing alloying elements as a function of oxidation time (a) without Sb and (b) with Sb. (The numbers in the figure correspond to the chemical compositions in Table I.)

simultaneously, and the weight change in the present experiment is the summation of decarburization (weight loss) and oxidation (weight gain), because the TG setup does not record decarburization and oxidation independently. The weight loss observed in the present experiments occurs because the relative rate of decarburization is faster than that of oxidation, and the degree of weight loss increases with increasing Si and P contents and decreases with Sb addition. The role of P, Si, and Sb on the oxidation of IF steels has been reported in a previous article.^[13] The results indicated

that Si and P accelerate and Sb suppresses the oxidation of IF steels. The chemical compositions among TRIP and IF steels are close except for the C content. It may, therefore, be concluded that Si and P increased the decarburization rates, whereas Sb decreased the decarburization rate. However, the way in which alloying elements affect the decarburization and oxidation has not been investigated. Therefore, it is necessary to understand the mechanisms of decarburization and oxidation and the effect of alloying element additions on decarburization and oxidation behavior.

B. Decarburization

The mechanism of decarburization has been extensively studied and is well understood, as summarized by Birks *et al.*^[18] The existence of a porous external scale is a precondition for decarburization to occur. This could not be unambiguously confirmed in the current characterization of surfaces and cross sections of the oxide scales due to the limits of resolution, but there was also no evidence that a dense uncracked protective oxide scale was present. For the current alloys, an intercritical annealing temperature of 843 °C was used; this would correspond to the alloy being at the $\alpha + \gamma/\gamma$ boundary, as shown in Figure 5(a). As carbon is lost, a concentration profile, schematically shown in Figure 5(b), will be expected to be established, in which the removal of carbon is coupled with movement of the $\alpha + \gamma/\gamma$ boundary. The term C_s is the concentration of carbon at the interface of ferrite and scale, $C_{\alpha/\gamma}$ is the concentration of carbon at the interface between ferrite and steel, and C_0 is the concentration in the bulk steel.

The following steps would be needed to remove the carbon: (1) steam/oxygen transport from the bulk gas flow through a gas-solid boundary layer to the scale surface, (2) steam/oxygen transport through the scale by diffusion through pores and cracks in the oxide scale,

(3) carbon reaction with steam/oxygen to form carbon monoxide, (4) carbon transport through the α layer to the α/scale interface, (5) movement of the $\alpha/\gamma + \alpha$ interface, and (6) carbon monoxide transfer from the scale-metal interface to the scale/gas interface *via* pores and cracks.

Under the present experimental conditions, a ferrite phase is formed during the decarburization process. As a first approximation, we will make the following assumptions. (1) The external scale is thin and is porous enough that it does not cause any hindrance to gas species from entering or escaping the surface and, therefore, steps (2) and (6) are considered to be fast. (2) The movement of the ferrite/ferrite + austenite phase boundary is not interface reaction controlled, *i.e.*, it is controlled by the diffusion of carbon and the interfacial equilibrium is maintained at all times.

The thickness of the ferrite region, x , can thus be calculated through the following equation:^[19]

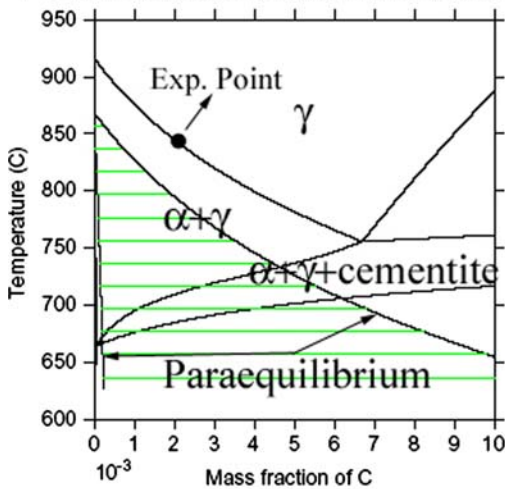
$$x = 2K\sqrt{D_C t} \quad [1]$$

where D_C is the intrinsic diffusion coefficient of carbon in ferrite, which can be obtained from the literature,^[20] t is the time, and K in Eq. [1] is a dimensionless constant, which can be obtained from Eq. [2]:

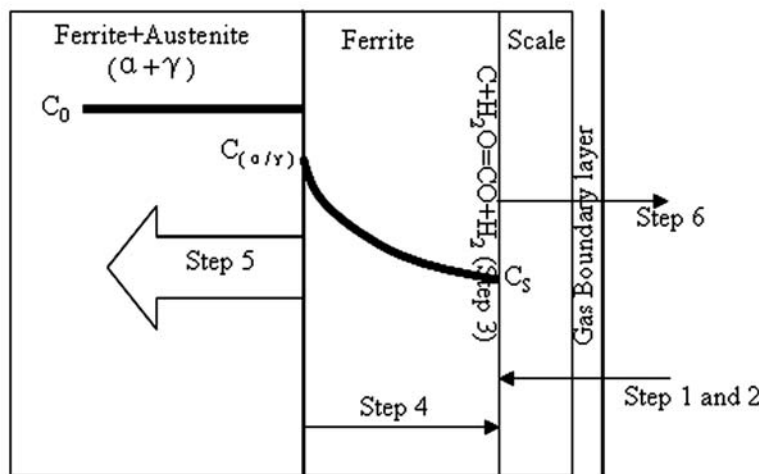
$$\frac{C_S - C_{\alpha/\gamma}}{C_{\alpha/\gamma} - C_0} = K\sqrt{\pi} \exp(K^2) \text{erf}(K) \quad [2]$$

where C_S is the carbon concentration on the α surface, which is assumed to be zero; C_0 is the bulk carbon concentration; and $C_{\alpha/\gamma}$, the carbon concentration in α at the $\alpha/\gamma + \alpha$ interface, can be estimated by Thermo-Calc (Thermo-Calc Software, Stockholm).^[21] It should be noted that the diffusivity of C (interstitial element) is much higher than that of Si, Al, and Mn (substitutional elements), so it is reasonable to assume that only C is mobile, whereas Si, Al, and Mn remain essentially in

THERMO-CALC (2007.11.14:17.00) :
 DATABASE:TCFE2
 P=1E5, N=1., W(SI)=5E-3, W(MN)=2E-2, W(AL)=5E-3;



(a)



(b)

Fig. 5—(a) Carbon isopleth for TRIP steel. (b) Schematic of decarburization mechanism.

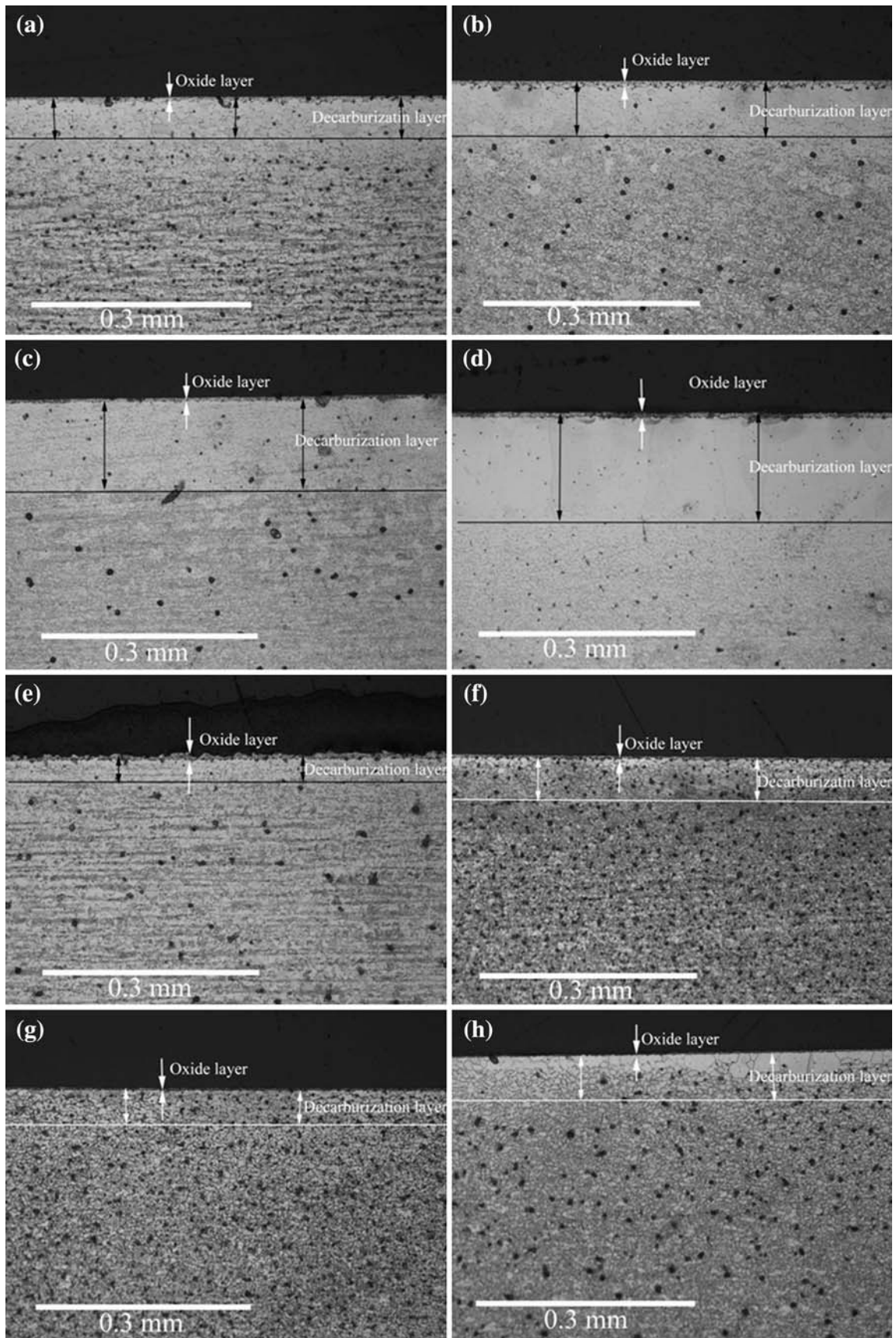


Fig. 6—Optical micrographs of cross sections etched with nital. (The letters in (a), (b), (c), (d), (e), (f), (g), and (h) correspond to samples of steel 1, 2, 3, 4, 5, 6, 7, and 8, respectively.)

their original positions. Unfortunately, the distribution of the substitutional elements would depend on prior processing and, therefore, their distribution is difficult to determine, which may result in some uncertainty in the value of $C_{\alpha/\gamma}$. A value corresponding to paraequilibrium, which refers to the concept that the diffusion kinetics of substitutional elements Mn and Si is much slower than that of the interstitial element C, [22] was used in the current study.

Figure 6 shows a series of optical micrographs of the etched cross sections of exposed specimens (30 minutes) containing different alloying elements under $P_{H_2O}/P_{H_2} = 0.13$ at 843 °C. As indicated, the decarburization layer has larger grains and appears to be free of pearlite, which is in agreement with an earlier article, [17] and the coarse grains are a result of decarburization-controlled ferrite growth into a duplex ferrite/austenite structure that starts at the surface and proceeds toward the core of the sample. The depths of the decarburization layer were estimated by the averaged value of ten measurements based on different micrographs, and the results are listed in Table II. As can be seen, the depth varies with chemical composition, and Si and P additions seem to result in a thick decarburized layer, whereas a Sb addition apparently decreased the decarburization layer thickness, *i.e.*, Si and P can increase the decarburization. This is consistent with the aforementioned TG results, which indicated that the decarburization rate increased with increasing Si and P contents, and an Sb addition suppressed the decarburization rate.

Equations [1] and [2] were used to calculate the depth of the decarburization layer, and the predicted depth is shown in Figure 7 along with the experimentally measured values. It should be pointed out that the adopted model is based on Fick's second law for the case of a semi-infinite slab, and is obtained by evaluating the dimensionless factor (K), which depends on the concentration of carbon ($C_{\alpha/\gamma+\alpha}$) at the $\alpha/\gamma + \alpha$ interface. The $C_{\alpha/\gamma+\alpha}$ was calculated by Thermo-Calc software [21] by considering a Fe-C-Si-P system. The calculated results are 1.11×10^{-2} , 1.16×10^{-2} , 1.41×10^{-2} , and 1.70×10^{-2} wt pct for steels 1, 2, 3, and 4, respectively. As can be seen from Figure 7, the predicted depths show large discrepancies with respect to the experimental measurements. These discrepancies could be caused by a number of factors. First, as mentioned earlier, there is an uncertainty in the distribution of the substitutional elements, which would influence the term $C_{\alpha/\gamma+\alpha}$ in Eq. [2]. Second, the diffusion coefficient of carbon could be affected by the presence of Si (and perhaps P).

In order to determine the effect of a Si addition on the diffusion coefficient of carbon, the present study back-calculated the diffusion coefficient of carbon using the measured decarburization depths by Eq. [1]. Figure 8 shows the back-calculated values according to Eqs. [1] and [2]. It indicates that the Si addition can increase the diffusion coefficient of carbon in steels both with and without Sb, from 2.63×10^{-11} m²/s for steel containing 0.5 pct Si to 7.28×10^{-11} m²/s for steel containing 1.5 pct Si, and from 1.28×10^{-11} m²/s for steel containing 0.5 pct Si and 0.03 pct Sb to 1.94×10^{-11} m²/s for steel containing 1.5 pct Si and 0.03 pct Sb, respectively.

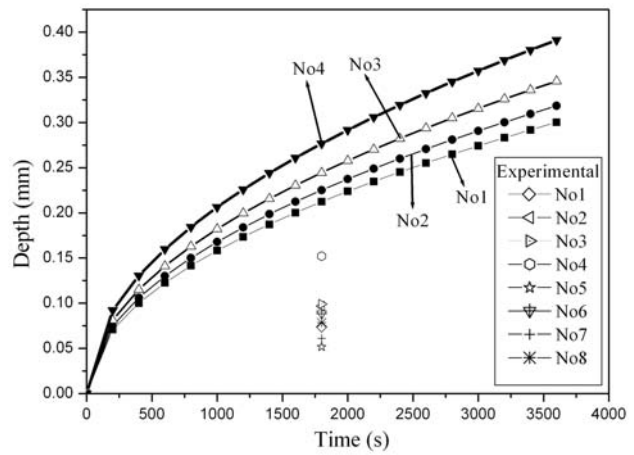


Fig. 7—A comparison between predicted and the measured decarburization depths. (The numbers in the figure correspond to the chemical compositions in Table I.)

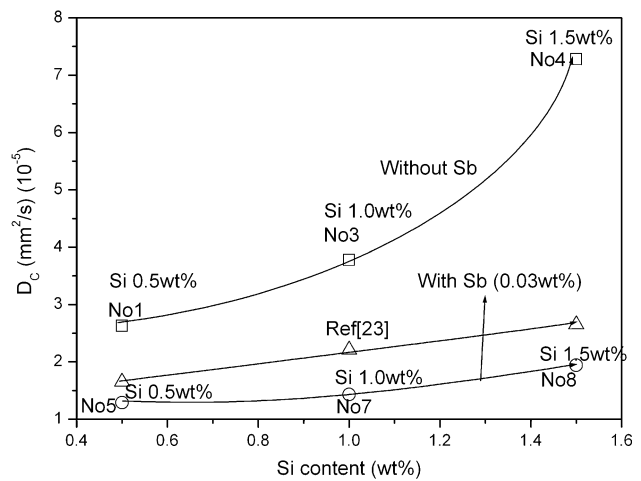


Fig. 8—Back-calculated diffusion coefficients of carbon as a function of silicon content. (The numbers labeled in the figure correspond to chemical compositions in Table II.)

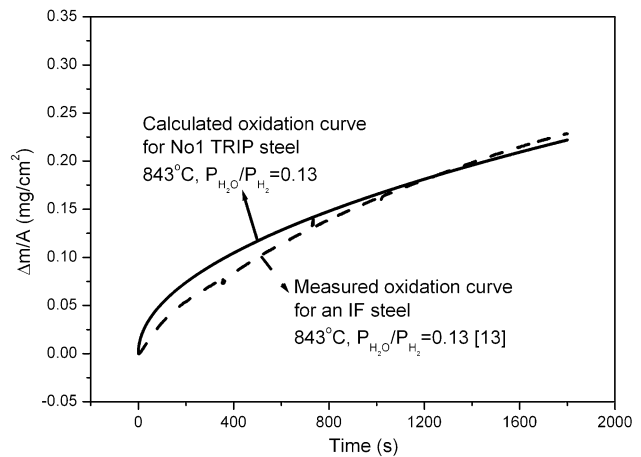


Fig. 9—A comparison of calculated oxidation curve for TRIP steel 1 and measured oxidation curve for an IF steel [13] under $P_{H_2O}/P_{H_2} = 0.13$ at 843 °C.

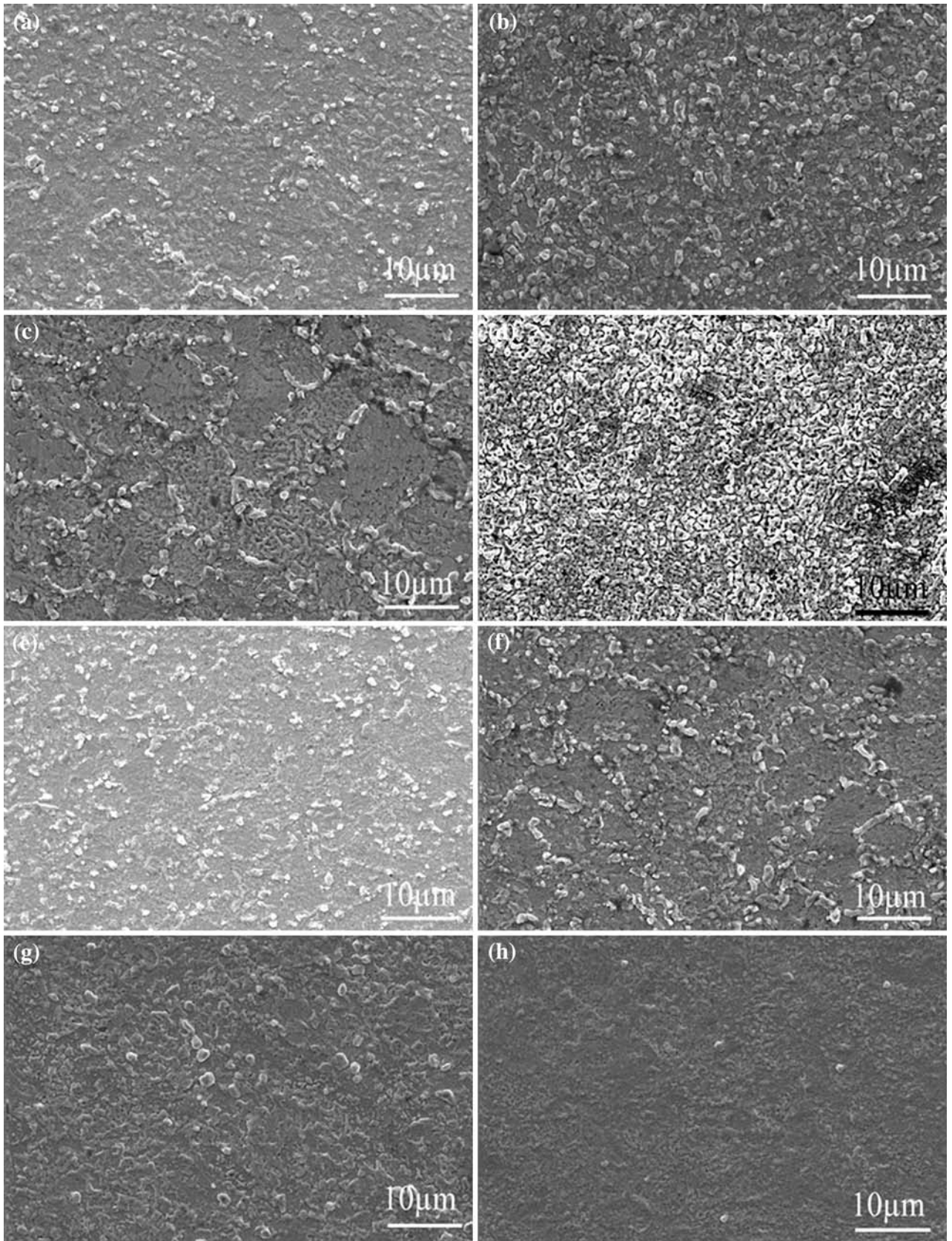


Fig. 10—Surface morphologies of TRIP steels after oxidation under $P_{H_2O}/P_{H_2} = 0.13$ at 843 °C. (The letters in (a), (b), (c), (d), (e), (f), (g), and (h) correspond to samples of steel 1, 2, 3, 4, 5, 6, 7, and 8, respectively.)

This is in agreement with a previous article, which showed that the diffusion coefficient of carbon increases with increasing Si content, from $1.65 \times 10^{-11} \text{ m}^2/\text{s}$ for steel containing 0.5 pct Si to $2.65 \times 10^{-11} \text{ m}^2/\text{s}$ for steel containing 1.5 pct Si.^[23,24] These values are plotted in Figure 8, along with those estimated in the current

investigation. The increasing diffusion coefficient of carbon has been explained by Darken's experiment, in which the C activity coefficient in iron was increased by Si.^[25]

C. Oxidation of TRIP Steels

Considering that the diffusion coefficient of carbon is much higher than that of Si, Al, and Mn, it is reasonable to assume that only C is mobile, whereas Si, Al, and Mn may remain in their original positions, *i.e.*, the oxidation of steel involves not C but Si, Al, and Mn. In view of the fact that the TG setup used in the present experiment does not record decarburization and oxidation independently, the mass increase due to oxidation, Δm (mg/cm^2) was thus estimated by Eq. [3]:^[18]

$$\Delta m = k_p t^{1/2} \quad [3]$$

where k_p ($\text{mg}/\text{cm}^2/\text{s}^{1/2}$) is the parabolic rate constant, which has been evaluated in a previous article.^[17] The curve for TRIP steel 1 due to oxidation under $P_{\text{H}_2\text{O}}/P_{\text{H}_2} = 0.13$ at 843 °C was thus computed and is shown in Figure 9. Figure 9 also shows the experimental weight changes of an IF steel as a function of time.^[13] As can be seen, the measured weight gain due to oxidation is in agreement with the computed values. In view of the

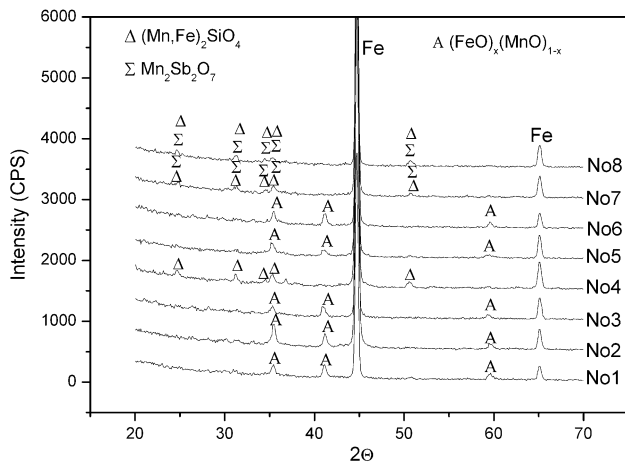


Fig. 11—G-XRD patterns of oxidized TRIP steels surfaces. (The numbers in the figure correspond to the compositions in Table I.)

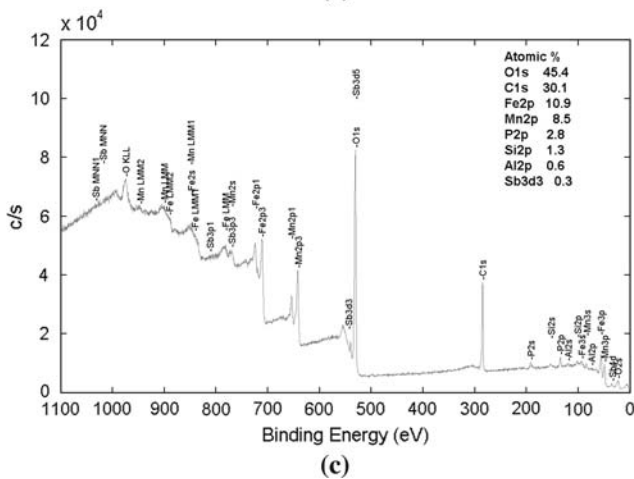
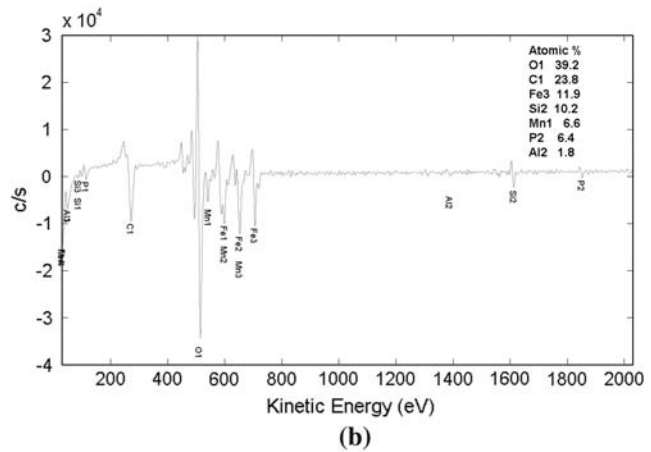
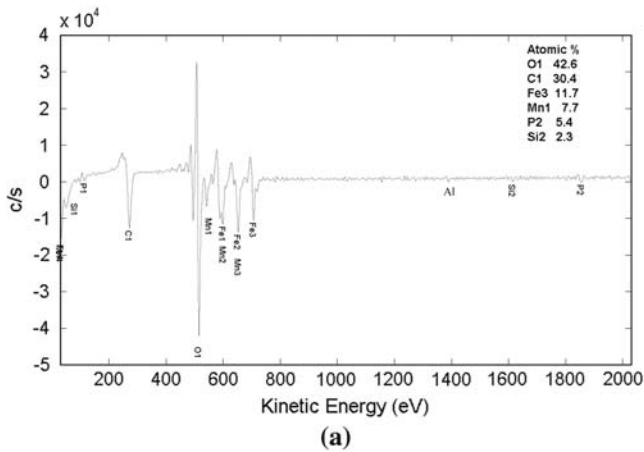


Fig. 12—AES spectra of samples of steel (a) 5 and (b) 8, and (c) XPS spectra of sample of steel 5 oxidized at 843 °C with $P_{\text{H}_2\text{O}}/P_{\text{H}_2} = 0.13$.

fact that the chemical compositions among TRIP and IF steels are close except for the C content, it is therefore reasonable to assume that the oxidation rates for both TRIP and IF steels are essentially the same. This suggests that oxidation proceeds independently of decarburization. It should be pointed out that the oxidation may involve both external and internal oxidation under the present experimental conditions, and that the internal oxidation is of greater importance than the external oxidation.

1. External oxidation

The surface morphologies of the specimens after oxidation were documented using the SEM in secondary electron mode; the results are shown in Figure 10. The small amounts of alloying element additions have significant effects on surface morphologies after oxidation. Two types of oxide evolution can be observed in Figure 10. The first type involves oxides that are primarily distributed at the alloy grain boundaries, including steels 1, 2, 3, 5, and 6. In the second type, including steels 4, 7, and 8, there are no obvious grain-boundary ridges observed, whereas continuous (4) or discontinuous (7 and 8) patchy nodules were observed. A significant difference in EDS analysis also exists between the two types, with obvious Mn enrichment in oxides formed on the grain boundaries for the first type of oxides, whereas only Fe was detected for the patchy nodules, and Mn-, Si-rich oxides were mainly distributed around the nodules. It is noteworthy that the EDS results for specimens 2 and 6 showed the oxide ridges contain some phosphorus.

Figure 11 shows the G-XRD patterns for steels of different chemical compositions. As can be seen, the phases precipitated on the surface change with increasing Si or Sb additions. The oxides on alloys with low Si addition are composed primarily of $(\text{FeO})_x(\text{MnO})_{1-x}$,

which are mainly precipitated on alloy grain boundaries according to the surface morphologies, whereas traces of $(\text{Mn, Fe})_2\text{SiO}_4$ were observed in the case of steels containing a high amount of Si. The structure of the Sb-oxide phase cannot be unambiguously established, but the glancing-angle X-ray peaks are closest (albeit weak) to $2\text{MnO}\cdot\text{Sb}_2\text{O}_5$. The reason for forming Sb_2O_5 rather than Sb_2O_3 is not clear. The latter is expected to be thermodynamically stable. It should be pointed out that no Al-oxide peaks are clearly discernable, as shown in Figure 11. This is probably because of the fact that the amount of Al oxides is small and is lower than the detection limits of G-XRD. On the other hand, Si oxide may appear as an amorphous phase.^[26,27] It should be noted that Fe oxides are not thermodynamically stable under the experimental conditions; however, some FeO may be formed in $(\text{Mn, Fe})_2\text{SiO}_4$ or $(\text{FeO})_x(\text{MnO})_{1-x}$.

Figures 12(a) and (b) show the Auger spectra characteristic of the surface chemistry of steels 5 and 8 after oxidation. According to the standard spectra,^[28] they indicated that Fe, Mn, Al, P, and Si appeared on the surface. It should be noted that the spot size used was $100\ \mu\text{m}$, *i.e.*, the signals obtained are the averaged values. The amount of Si for steel 8 was found to be higher, whereas the amount of Mn was smaller than that for steel 5, and the Al signal is very weak. The Fe signal is very strong, which may be metal from the matrix or oxide. In order to specify detected-element distribution, Auger electron maps were used and the results are shown in Figure 13. The maps were individually optimized for maximum contrast. It indicates that Mn is mainly distributed along alloy grain boundaries, *i.e.*, the ridges are mainly Mn rich oxides. The Fe signal is strong across the interior grain surface but is very weak along grain-boundary ridges, indicating that the FeO content in $(\text{FeO})_x(\text{MnO})_{1-x}$ that is detected by G-XRD is very low. The Al signal is very weak across the whole surface.

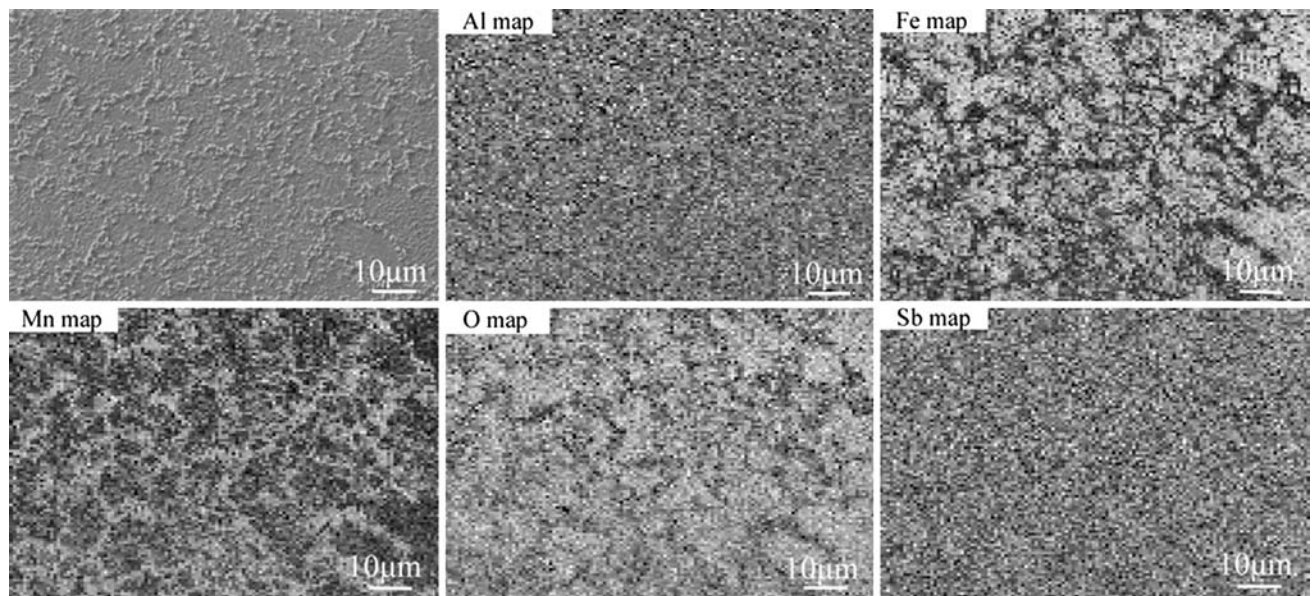


Fig. 13—AES maps of TRIP steel 5 oxidized at 843 °C under $P_{\text{H}_2\text{O}}/P_{\text{H}_2} = 0.13$ for 30 min.

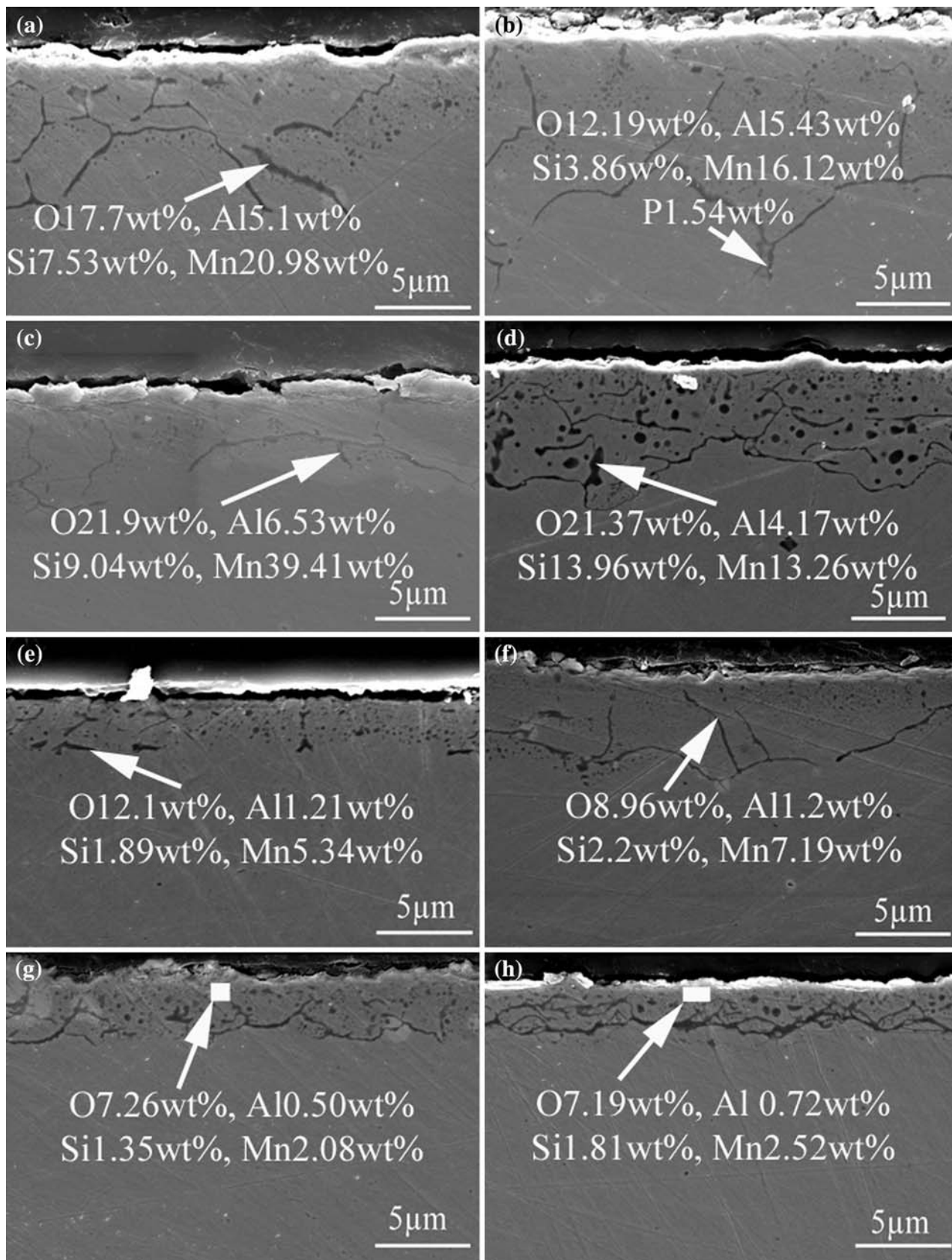


Fig. 14—SEM observation of cross sections of TRIP steels oxidized at 843 °C under $P_{H_2O}/P_{H_2} = 0.13$ for 30 min. (The letters in (a), (b), (c), (d), (e), (f), (g), and (h) correspond to samples of steel 1, 2, 3, 4, 5, 6, 7, and 8, respectively.)

The AES map of O shows a strong signal across interior grains, whereas a weak signal is observed along grain boundaries. This may suggest that the oxides at the grain interior surfaces contain higher oxygen content, probably Al_2O_3 , SiO_2 . The AES map of Sb indicates this element is uniformly distributed across the whole surface.

Using XPS, the oxidation states of Mn, Si, Sb, and Al can be determined and the surface species identified where information on their binding energy was available, as can be seen from Figure 12(c). These results indicate that the binding energies for Mn, Al, O, Sb, and Si are 641.9, 74.7, 531.6, 537, and 102.7 eV, respectively, corresponding to Mn^{2+} , Al^{3+} , O^{2-} , Sb^{5+} , and Si^{4+} , respectively, according to the standard XPS spectra.^[29] This is consistent with the G-XRD results.

2. Internal oxidation

The SEM observations of the polished cross sections of TRIP steels after oxidation revealed that the oxides formed along the alloy grain boundaries and reached as deep as 5.2 to $\sim 8.3 \mu\text{m}$ for TRIP steels containing 0.02 pct P, compared to $9.9 \mu\text{m}$ for a TRIP steel containing 0.08 pct P, as can be seen from Figure 14 and Table II. However, the oxides formed exist at a depth of less than $3.5 \mu\text{m}$ for TRIP steels containing 0.03 pct Sb, except for steel 6, where the oxides reached a depth of $5.0 \mu\text{m}$. The density of oxides for TRIP steel 4 is quite high compared with the steels 1, 2, and 3, *i.e.*, Si addition promotes internal oxidation. This is consistent with an earlier article.^[13] It is noteworthy that the grain boundaries in question are most likely the boundaries between the new ferrite grains that grow due to decarburization, because the penetration of decarburization is significantly faster than the penetration of internal oxidation. The EDS results indicate that the oxides along the grain boundaries are Mn-, Al-, and Si-rich oxides, and that some P was also found for TRIP steels 2 and 6. However, the oxides on the surface are mainly composed of Mn-oxides. The amounts of Al- and Si-oxides are small due to the small bulk concentrations of Al and Si. Furthermore, the elements Al and Si have a higher affinity for oxygen compared

with that for Mn; therefore, Al and Si were first oxidized when the steel was exposed to the oxidizing atmosphere ($P_{\text{H}_2\text{O}}/P_{\text{O}_2} = 0.13$), which resulted in formation of the subsurface oxides.

The XPS depth profiles (element intensities) for steel 5 are shown in Figure 15. The thicknesses of Fe-, Si-, and Al-oxide are several nanometers, which correspond to the external oxidation layer. The signal for Mn, however, was found to remain constant in the measured range of depth. This is mainly caused by the inward diffusion of oxygen, resulting in internal oxidation. This is consistent with SEM results on cross sections.

The combined results from TG, the surface characterization by SEM, XPS, and AES, and cross-sectional micrographs by SEM and XPS give the following information. (1) A thin external oxidation layer several nanometers thick exists, which consists of oxides of Si, Al, or Fe or the solid solutions or compounds formed by these oxides. (2) The oxide ridges that appear on the grain boundaries of TRIP steels could be the result of fast-path grain-boundary diffusion. Because decarburization is expected to be rapid, the grain boundaries responsible for the transport of O as well as the substitutional elements, mainly Mn, are likely the newly formed ferrite grain boundaries (as a result of decarburization) that are responsible for the kinetics of ridge evolution. (3) The increased P concentration results in an increase in decarburization and oxidation, and the results are consistent with the TG results between TRIP steels 1 and 2, as well as between 5 and 6 (Figure 4). They are also in agreement with surface morphologies after oxidation (Figure 10). (4) The decarburization rate increased with increasing Si content under the present experimental conditions. (5) The Sb addition obviously decreases the decarburization depth and oxidation depth, which is in agreement with the TG results (Figure 4) and the surface morphologies after oxidation (Figure 10).

D. Effect of Si on Weight Change of TRIP Steels

The effect of Si content on weight changes vs oxidation time is shown in Figure 16 for steels that do

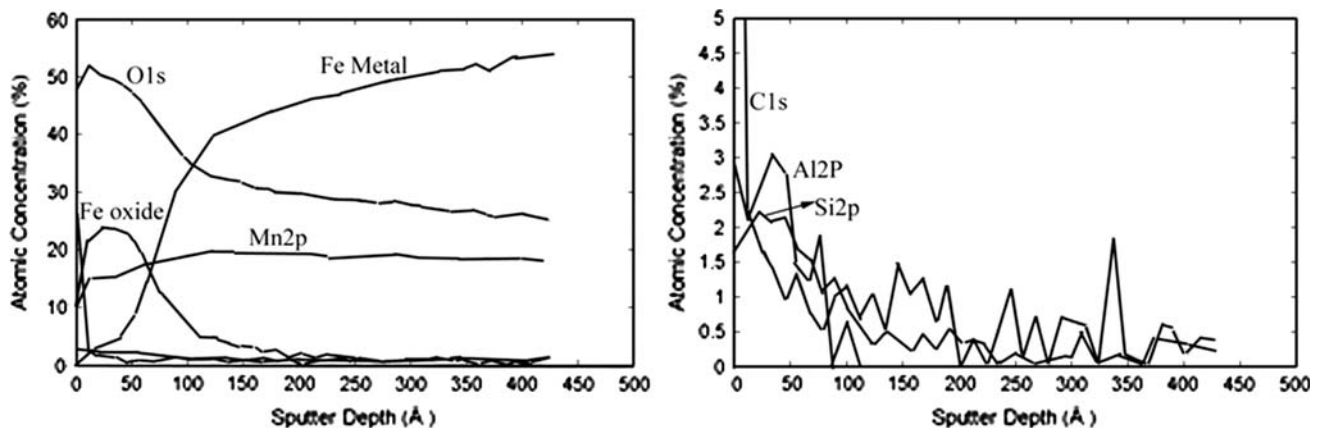


Fig. 15—Depth profiles of TRIP steel 5 oxidized at 843 °C under $P_{\text{H}_2\text{O}}/P_{\text{H}_2} = 0.13$ for 30 min.

not contain Sb (Figure 16(a)) and those that do (Figure 16(b)). It can be seen that the weight losses increase with increasing Si content in all cases. According to the experimental observation shown in Figure 6,

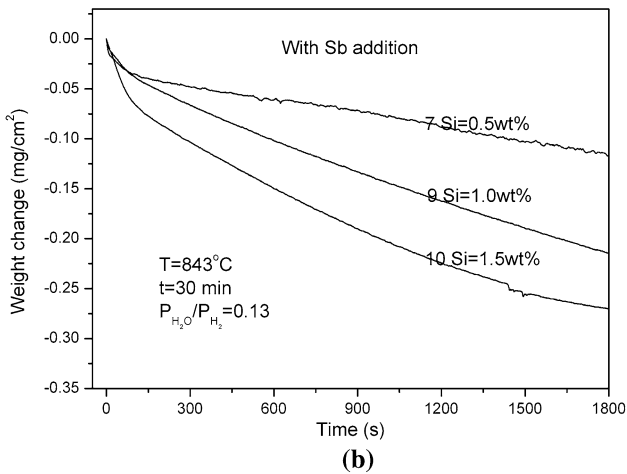
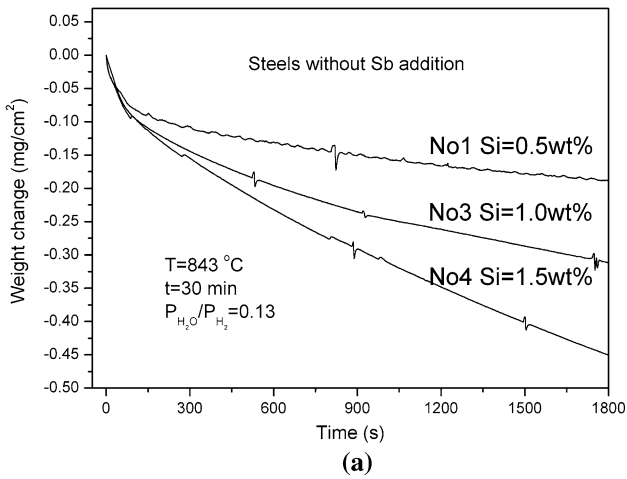


Fig. 16—The effect of Si content on the weight change of TRIP steels (a) without and (b) with Sb addition. (The numbers in the figure correspond to the chemical compositions in Table I.)

the decarburization depths are 73.9, 99.1, and 152.0 μm for TRIP steels containing 0.5 pct (steel 1), 1.0 pct (steel 3), and 1.5 pct Si (steel 4), respectively, and similar results are observed for TRIP steels containing Sb (5, 7, and 8), as can be seen from Table II. The increased weight loss could also be caused by a decrease in internal oxidation, but such an effect is not apparent from the present results. The Si contents less than that needed to form continuous oxide layers have been shown to increase the internal oxide density.^[13] The oxide density appears in this study also to increase with increasing Si content (Figure 14). It can therefore be concluded that decarburization rate increases with increasing Si content. It is also noteworthy that, resulting from the volume mismatch between oxides and iron, an outward plastic flow of iron occurred, as can be seen from Figure 17. The iron extruded to the surface is expected to be proportional to the volume of internal oxides.^[30] This phenomenon has been reported in an earlier publication.^[13] As discussed previously, the increased decarburization rate occurs because the diffusion coefficient of carbon increases with increasing Si content (Figure 8).

A summary of the effects of Si addition on the decarburization and oxidation is shown in Table III, indicating that the addition of Si increases the decarburization depths and has no obvious effect on decreasing internal oxidation. The G-XRD (Figure 11) and XPS analysis (Figure 12(c)) indicate that the surface oxide chemistry evolved from $(\text{MnO})_x \cdot (\text{FeO})_{1-x}$ to $(\text{Fe, Mn})_2\text{SiO}_4$ with increasing Si from 0.5 to 1.5 pct.

E. Effect of Sb on Weight Change of TRIP Steels

Figure 18 describes the effects of an Sb addition on the weight changes of TRIP steels, and it can be seen that the weight change increase becomes less negative with a small addition of Sb. This could be caused by either a decrease in decarburization rate or an increase in the oxidation rate. The investigation of surface morphologies (Figure 10) and cross sections (Figure 14) indicates that Sb suppresses both the internal oxidation and decarburization. This is consistent with an earlier

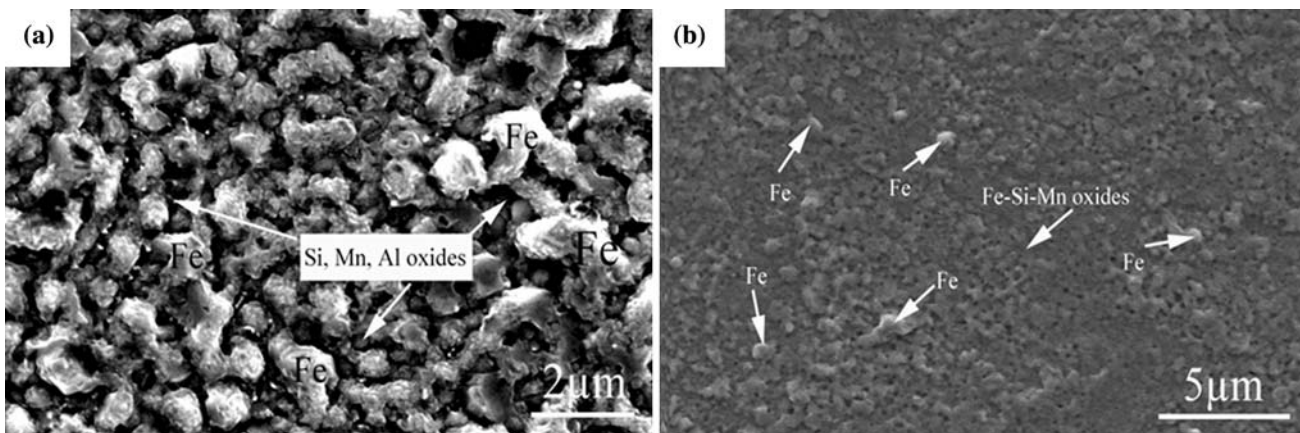


Fig. 17—Surface morphologies of steel (a) 4 and (b) 8 oxidized at 843 °C with $P_{\text{H}_2\text{O}}/P_{\text{H}_2} = 0.13$ for 30 min.

Table III. Effect of Si, P, and Sb Additions on Decarburization and Oxidation of TRIP Steels

Effect of:	TG Curve	Degree of Internal Oxidation	Degree of Decarburization	Surface Oxidation
Increasing of Si	decrease (Fig. 16)	increase (Fig. 14 and Table II)	increase (Fig. 6 and Table II)	from oxide ridges to isolated ferrite (Fig. 10)
Increasing of P	decrease (Fig. 18)	increase (Fig. 14 and Table II)	increase (Fig. 6 and Table II)	larger size of oxides was found (Fig. 10)
Increasing of Sb	increase (Fig. 19)	decrease (Fig. 14 and Table II)	decrease (Fig. 6 and Table II)	density of oxides decreases (Fig. 10)

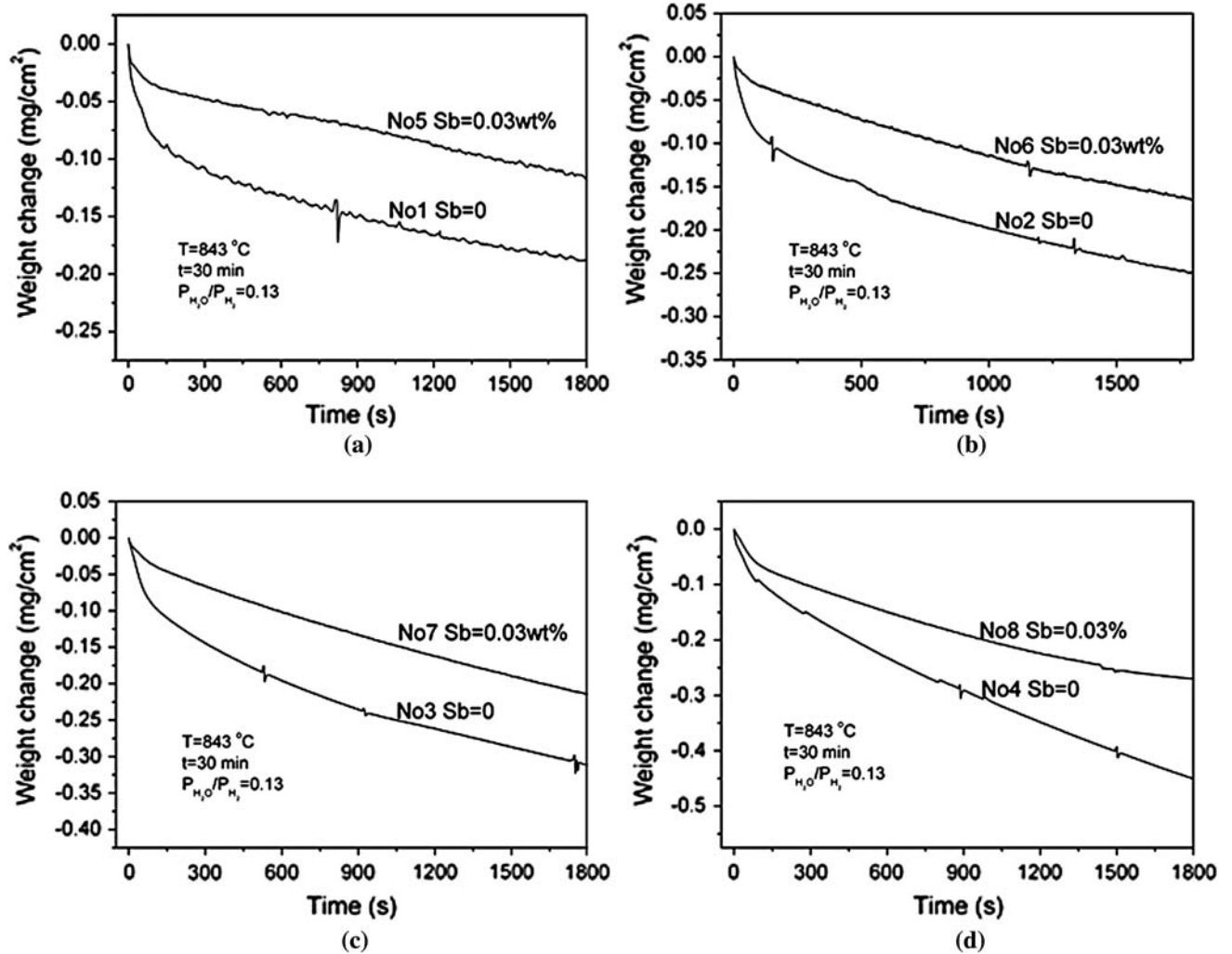


Fig. 18—The effect of Sb addition on the weight change of TRIP steels with (a) 0.5 pct Si and 0.02 pct P, (b) 0.5 pct Si and 0.08 pct P, (c) 1 pct Si and 0.02 pct P, and (d) 1.5 pct Si and 0.02 pct P. (The numbers in the figure correspond to the chemical compositions in Table I.)

article, which showed that a small amount of Sb addition decreased both the external and internal oxidation.^[13] Therefore, it is likely that the effect of Sb on decreasing the weight loss in Figure 18 is due to a decrease in the decarburization rate. A summary of the effect of an Sb addition on the decarburization and oxidation is shown in Table III, indicating that the Sb decreased the decarburization and oxidation. A comparison of the relative intensity of the G-XRD peaks

indicated that the oxide thickness on the surface was also decreased.

It is well known that Sb is a surface active element that would occupy the adsorption surface sites, and this may decrease the oxygen permeability.^[13,31,32] The segregated Sb layer on the surface and grain boundaries could thus block the outward diffusion of Mn or the inward diffusion of O. The internal oxidation and decarburization could thereby be suppressed. However,

under the present experimental conditions, $Mn_2Sb_2O_7$ is formed during the exposure, according to the G-XRD (Figure 11) and XPS results (Figure 12(c)), and therefore segregation during the experiment is not likely to play an important role. It is more likely that the $Mn_2Sb_2O_7$ acts as a diffusion barrier.

F. Effect of P on Weight Change of TRIP Steels

The weight loss increased with an increasing P addition, as shown in Figure 19. According to the measured decarburization layer and oxidation layer shown in Table III, P increased both the internal oxidation and decarburization. It is noteworthy that the EDS results for steels 2 and 6 showed that the oxide ridges contain some phosphorus. This is consistent with an earlier article,^[13] in which it was shown that P additions slightly accelerate the oxidation of IF steels.

Table III shows a summary of the effects of a P addition on decarburization and oxidation. As can be seen, it is obvious that a P addition increases both decarburization and oxidation.

G. Effect of Water Vapor Content on Weight Change of TRIP Steels

Figures 20 through 24 show the effects of water vapor content on TG, surface morphology, G-XRD patterns and cross sections of steels oxidized at 843 °C. The weight losses for steel 1 under different water vapor contents are comparable up to 300 seconds, followed by a decrease with the increasing water vapor contents shown in Figure 20(a). The weight changes for specimen steel 5 with a small Sb addition, however, show different results. It was found that a weight gain initially was observed under $P_{H_2O}/P_{H_2} = 0.01$ and 0.061, followed by a weight loss. It is noteworthy that the length of the weight gain period decreases with increasing water vapor content, and no weight gain was observed as the water vapor reaches $P_{H_2O}/P_{H_2} = 0.13$. From Figures 21 and 10(a), it can be seen that patches of nodules

consisting of Fe were formed, and oxide ridges consisting of $(FeO)_x(MnO)_{1-x}$ appeared with increasing water vapor content. Meanwhile, the patchy Fe nodules become faint. The Sb addition results in refinement of the patchy Fe nodules and the oxide distribution becomes more uniform. Figure 22 gives the G-XRD patterns, indicating that the intensity of oxides decreased with both decreasing water vapor content and Sb addition. The oxides were indexed as $(FeO)_x(MnO)_{1-x}$. Cross sections for unetched specimens and specimens etched by nital were examined by SEM and the results are shown in Figures 23 and 24; the depths of internal oxidation and decarburization layers are then examined and summarized in Table II, indicating that the depths of the oxide and decarburization layer decrease with decreasing water vapor content, and Sb obviously decreased the penetration depth. Figure 24 shows SEM images from selected etched specimens. As can be seen, the depth of the decarburization layer decreases with decreasing water vapor content. It should be noted that no obvious decarburization layer was detected for specimen 5 oxidized under $P_{H_2O}/P_{H_2} = 0.061$ and 0.01 (Figures 24(c) and (d)).

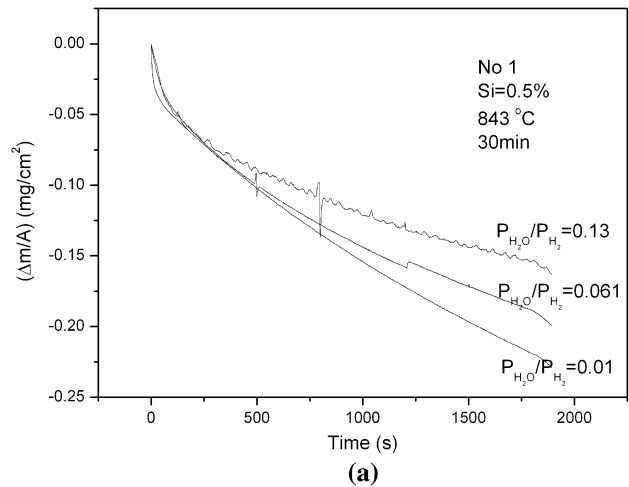


Fig. 19—Effect of P content on the weight change of TRIP steels oxidized at 843 °C under $P_{H_2O}/P_{H_2} = 0.13$ for 30 min. (The numbers in the figure correspond to the chemical compositions in Table I.)

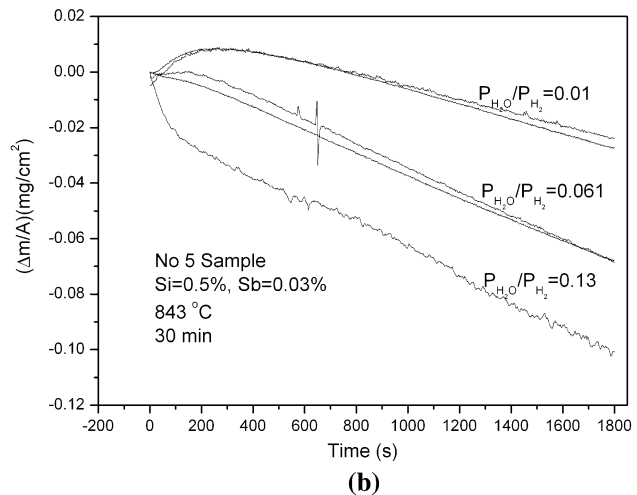


Fig. 20—Mass change of TRIP steels of samples of steel (a) 1 and (b) 5 under different water vapor contents.

As discussed in Section C, the oxidation and decarburization are independent and the oxidation rate is closely related to the water vapor content.^[13] As reported in a previous article, the mass transfer from bulk gas to the specimen surface and the dissociation of water vapor are not the controlling steps under the present experimental conditions. In the initial stage, oxidation takes place at the surface. It is to be expected that the chemical reaction controls the rate of oxidation. The rate of weight gain due to oxidation is expected to remain unchanged during this stage (less than 150 seconds). Once a thin external layer was formed, the diffusion of oxygen or cations is likely to be the controlling step. It has been reported that the diffusion is closely related to the oxygen solubility in Fe, which depends on the water vapor content.^[18,19] The rate of weight gain due to oxidation decreases with decreasing water vapor content. The water vapor content, however, has no influence on the decarburization rate, according to Eqs. [1] and [2]. The weight change that shows the summation of oxidation and decarburization, therefore, remains the same initially, followed by an increase with increasing water vapor content (Figure 20(a)).

It is known that Sb segregates on the steel surface and grain boundaries during the hot rolling process.^[31] In an

earlier article,^[13] it was reported that an Sb addition can suppress both external and internal oxidation due to a decrease in the local oxygen partial pressure by the oxidation of Sb under $P_{H_2O}/P_{H_2} = 0.13$. With further decreasing water vapor content, Sb may be present as a

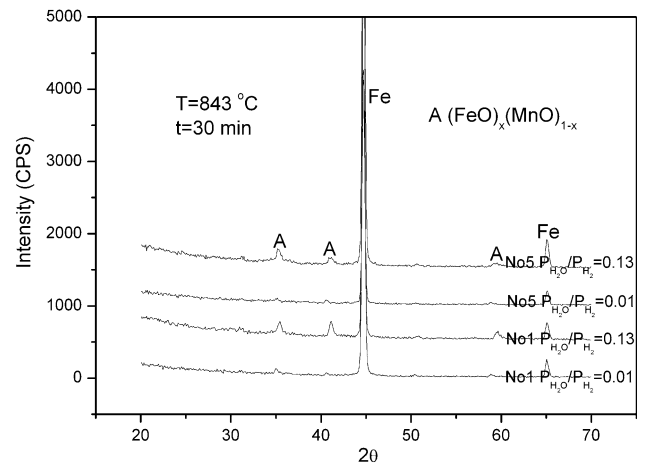


Fig. 22—G-XRD patterns of steels oxidized at 843 °C with $P_{H_2O}/P_{H_2} = 0.01$ and 0.13.

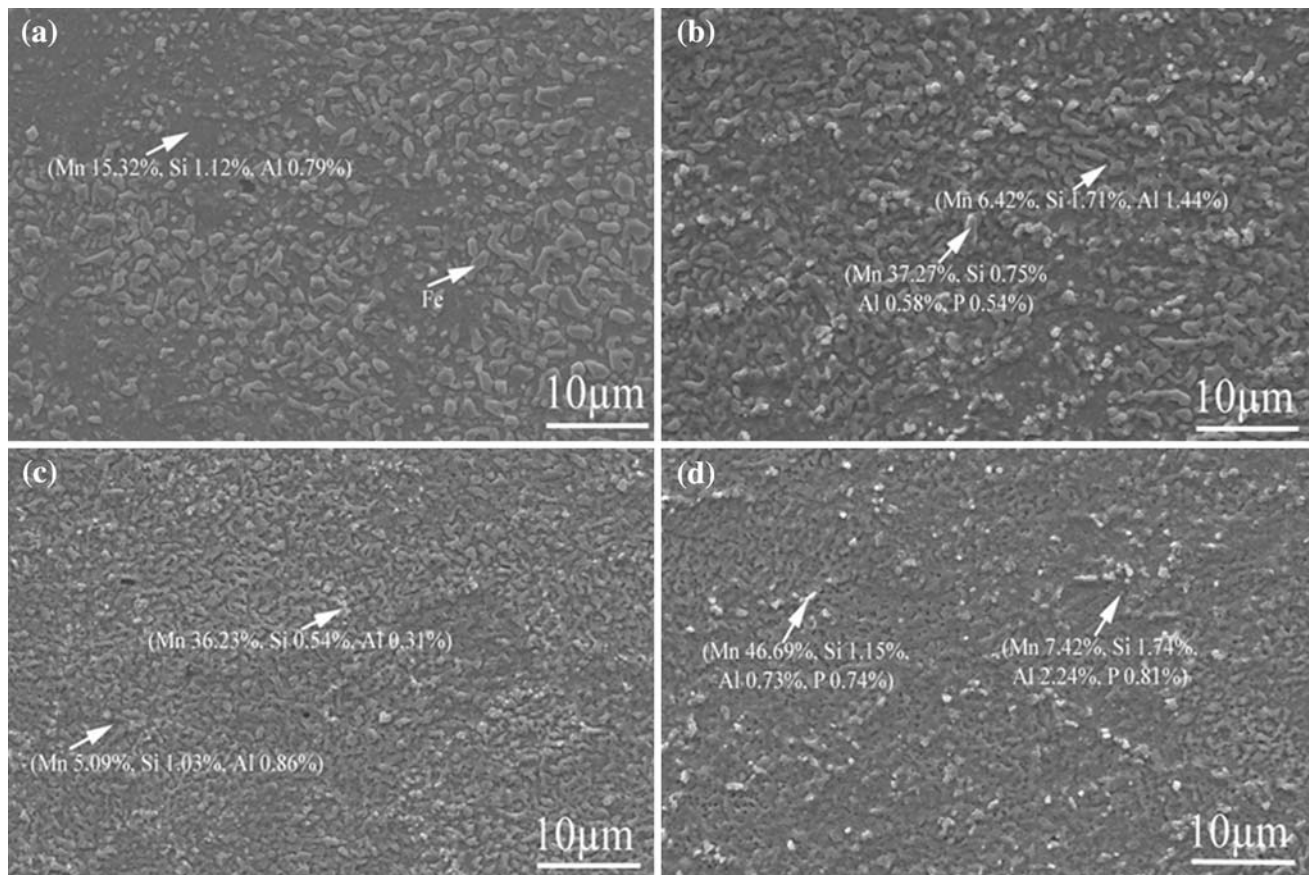


Fig. 21—Effect of water vapor content on surface morphologies (a) $P_{H_2O}/P_{H_2} = 0.01$, sample of steel 1; (b) $P_{H_2O}/P_{H_2} = 0.061$, sample of steel 1; (c) $P_{H_2O}/P_{H_2} = 0.01$, sample of steel 5; and (d) $P_{H_2O}/P_{H_2} = 0.061$, sample of steel 5.

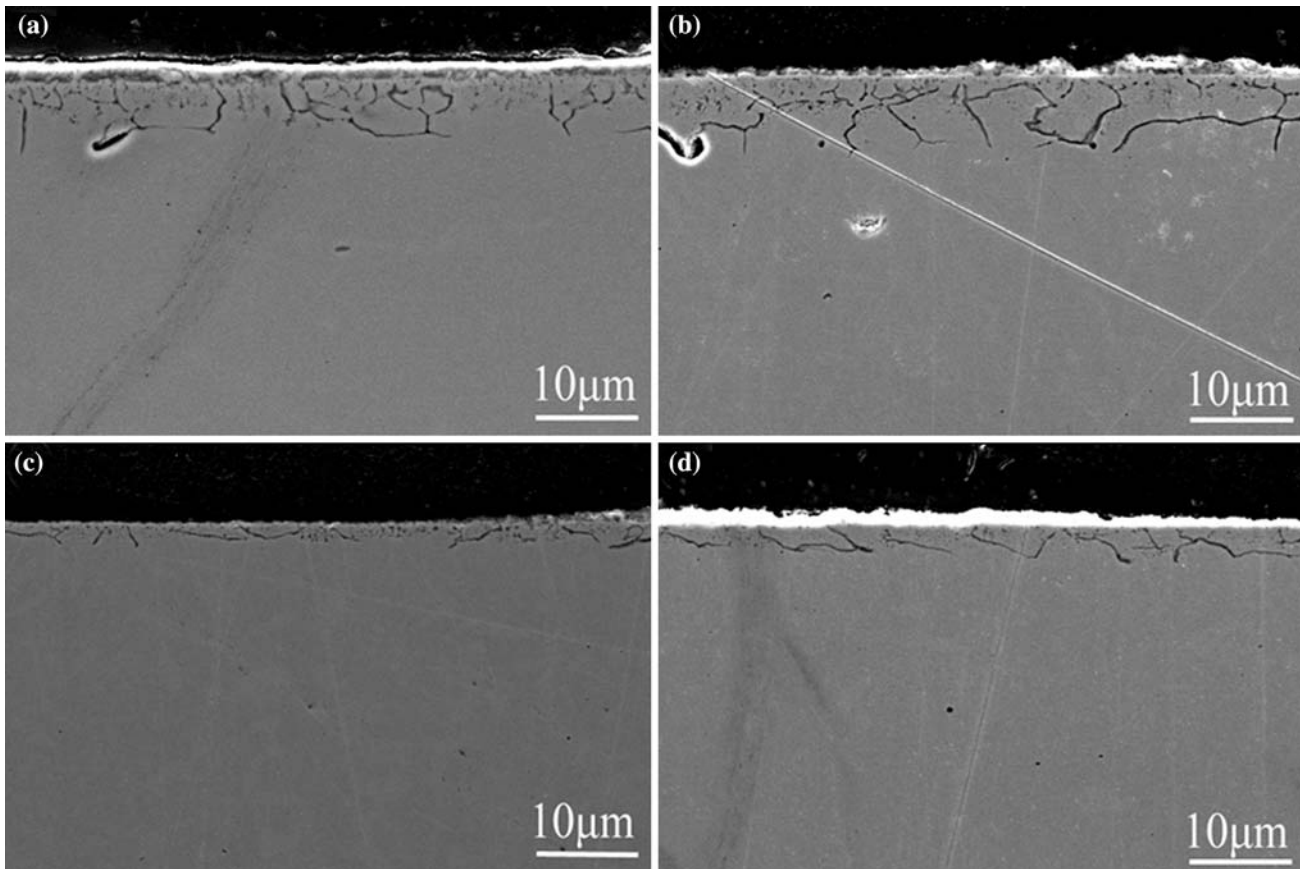


Fig. 23—Oxide layers of steels oxidized at 843 °C with $P_{H_2O}/P_{H_2} = 0.01$ for samples of steel (a) 1 and (c) 5, as well as $P_{H_2O}/P_{H_2} = 0.061$ for samples of steel (b) 1 and (d) 5.

metal layer on the steel surface, because Sb is a nobler metal than Fe, which is likely to occupy absorption surface sites to suppress the oxygen permeability and outward diffusion of metal cations.^[31,32] In the initial stage, chemical reaction occurring on the surface is the controlling step, and the decarburization is suppressed due to the presence of Sb. The TG curves, therefore, show a weight increase due to the dominance of the rapid rate of oxidation over the rate of decarburization. With increasing water vapor content, the oxygen permeability is increased. This may increase the decarburization, which could result in a dominance of rapid decarburization over the rate of oxidation. The TG curves correspondingly show weight losses under high water vapor contents. Once an external layer is formed, the oxidation is controlled by the inward diffusion of oxygen. The Sb plays a significant role in suppressing the internal oxidation in this situation.

IV. CONCLUSIONS

The oxidation and decarburization behavior for TRIP steels with different chemical compositions was

investigated by TG, G-XRD, OM, SEM, AES, and XPS techniques. The conclusions are as follows.

1. The weight change behavior (increase or decrease) of all the specimens depends on the summation of the decarburization and oxidation (both internal and external).
2. The G-XRD, AES, and XPS results indicate that the external layer was several nanometers in thickness and composed of $(MnO)_x(FeO)_{1-x}$ or $(Mn, Fe)_2SiO_4$ compounds that depend on the bulk silicon content. When Sb is added, traces of $Mn_2Sb_2O_7$ were observed. The EDS results indicate that the internal oxides are Mn-, Al-, and Si-rich oxides, and some P was found at grain boundaries for TRIP steels 2 and 6. The experimental results indicate that the decarburization and oxidation are mutually independent.
3. Increasing Si and P has the effect of increasing decarburization. The addition of Sb suppresses the decarburization and internal oxidation of TRIP steel under different water vapor contents.
4. Water vapor content has no obvious effect on decarburization but does have a pronounced effect on oxidation, and decreasing water vapor content decreases the oxidation rates.

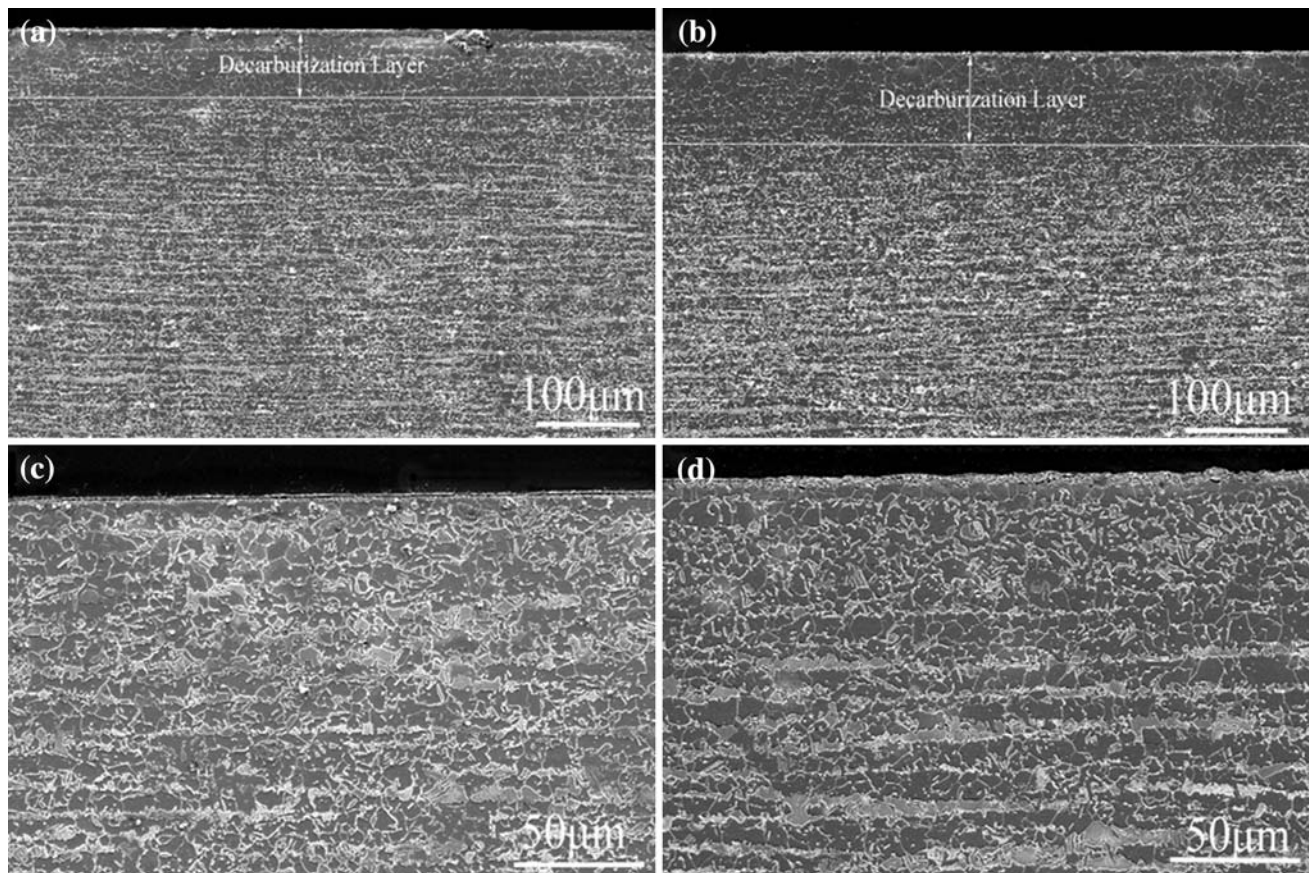


Fig. 24—Decarburization layers of steels oxidized at 843 °C with $P_{H_2O}/P_{H_2} = 0.01$ for samples of steel (a) 1 and (c) 5, as well as $P_{H_2O}/P_{H_2} = 0.061$ for samples of steel (b) 1 and (d) 5.

ACKNOWLEDGMENTS

The financial support from POSCO (Jeonnam, Korea) is acknowledged. T.L. Baum is acknowledged for her technical help during discussions during TG and SEM measurements. Special thanks are also extended to B. Webler, J. Nakano, and C. Thorning for instructive discussions. W. Jennings, Materials Science and Engineering, Case Western Reserve University (Cleveland, OH), is gratefully acknowledged for his help on AES and XPS analysis.

REFERENCES

1. H.K.D.H. Bhadeshia: *ISIJ Int.*, 2002, vol. 42, pp. 1059–60.
2. A. Perlade, O. Bouaziz, and Q. Furnemont: *Mater. Sci. Eng., A*, 2003, vol. 356, pp. 145–52.
3. B.L. Jones and P.N. Jones: *Scripta Metall.*, 1974, vol. 8, pp. 445–50.
4. E. Girault, A. Mertens, P. Jacques, Y. Houbaert, B. Verlinden, and J. Van Humbeeck: *Scripta Mater.*, 2001, vol. 44, pp. 885–92.
5. L. Allegra, R.G. Hart, and H.E. Townsend: *Metall. Trans. A*, 1983, vol. 14A, pp. 401–11.
6. C.E. Jordan, R. Zuhr, and A.R. Marder: *Metall. Mater. Trans. A.*, 1997, vol. 28A, pp. 2695–703.
7. P. J. Jacques, E. Girault, P. Harlet, and F. Delannay: *ISIJ Int.*, 2001, vol. 41, pp. 1061–67.
8. B.C. De Cooman, J. Mahieu, J. Maki, and S. Claessens: *Metall. Mater. Trans. A*, 2002, vol. 33A, pp. 2573–80.
9. M. De Meyer, D. Vanderschuren, and B. De Cooman: *ISIJ Int.*, 1999, vol. 39, pp. 813–22.
10. D.W. Suh, S.J. Park, C.S. Oh, and S.J. Kim: *Scripta Mater.*, 2007, vol. 57, pp. 1097–1100.
11. P.J. Jacques, E. Girault, A. Mertens, B. Verlinden, J.V. Humbeeck, and F. Delannay: *ISIJ Int.*, 2001, vol. 41, pp. 1068–74.
12. G. Lyudkovsky and P.K. Rastogi: *Metall. Trans. A*, 1984, vol. 15, pp. 257–60.
13. Z. Zhang, I.R. Sohn, G. Meier, F. Pettit, and S. Sridhar: *Metall. Mater. Trans. B*. DOI:10.1007/s11663-009-9238-y.
14. M. Jenko, F. Vodopivec, H.J. Grabke, H. Viefhaus, B. Pracek, M. Lucas, and M. Godec: *Steel Res.*, 1994, vol. 65, pp. 500–04.
15. R. Mast, H.J. Grabke, M. Jenko, and M. Lucas: *Mater. Sci. Forum*, 1996, vol. 207, pp. 401–04.
16. C. Thorning and S. Sridhar: *Philos. Mag.*, 2007, vol. 87, no. 23, pp. 1–21.
17. T. Baum, R.J. Fruehan, and S. Sridhar: *Metall. Mater. Trans. B*, 2007, vol. 38B, pp. 287–97.
18. N. Birks, G. Meier, and F. Pettit: *Introduction of High Temperature Oxidation of Metals*, 2nd ed., Cambridge University Press, Cambridge, United Kingdom, 2006, p. 151.
19. C. Wagner: *Z. Elektrochem.*, 1959, vol. 63, pp. 772–82.
20. C. Wert and C. Zener: *Phys. Rev.*, 1949, vol. 76, pp. 1169–75.
21. B. Sundman: *Proc. Symp. Thermodynamics, Kinetics, Characterization, and Modeling of Austenite and Decomposition*, E. Buddy Dam and Matthew J. Merwin, eds., TMS, Warrendale, PA, 2003, pp. 113–20.
22. M. Hillert and J. Agren: *Scripta Mater.*, 2004, vol. 50, pp. 697–99.
23. W.F. Gale, T.C. Totemeier, and J.C. Smithells: *Metals Reference Book*, Elsevier Butterworth-Heinemann, Burlington, MA, 2004, p. 680.
24. E. Schurmann, Th. Schmidt, and F. Tillmann: *Giesserei Forsch.*, 1967, vol. 19, p. 25.

25. L.S. Darken: *Trans. AIME*, 1949, vol. 180, pp. 430–38.
26. X.S. Li, S.I. Baek, C.S. Oh, S.J. Kim, and Y.W. Kim: *Scripta Mater.*, 2008, vol. 59, pp. 290–93.
27. X.S. Li, S. Baek, C.S. Oh, S.J. Kim, and Y.W. Kim: *Scripta Mater.*, 2007, vol. 57, pp. 113–16.
28. C.L. Hedberg: *Handbook of Auger Electron Spectroscopy*, 3rd ed., Physical Electronics, Inc., Chanhassen, MN, 1976, p. 142.
29. J. Chastain: *Handbook of X-Ray Photoelectron Spectroscopy*, Perkin-Elmer, Inc., Waltham, MA, 1992, p. 128.
30. J.E. Hammer, S.J. Laney, R.W. Jackson, K. Coyne, F.S. Pettit, and G.H. Meier: *Oxid. Met.*, 2007, vol. 67, pp. 1–38.
31. G. Lyudkovsky: *IEEE Trans. Magn.*, 1986, vol. 22, pp. 508–10.
32. I.R. Sohn, S.H. Jeon, H.J. Kang, and K.G. Chin: *Galvatech '07*, The Iron and Steel Institute of Japan, Japan, 2007, pp. 439–43.